JOURNAL OF SOLID STATE CHEMISTRY

Volume 179, Number 6, June 2006

CONTENTS

Regular Articles

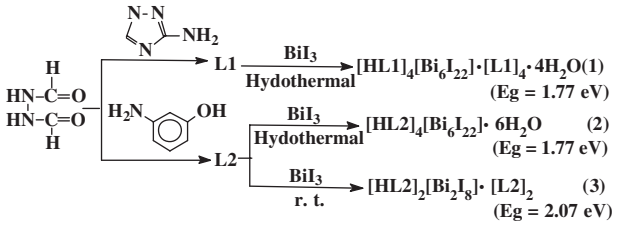

The reactions of two kinds of the substituted 1,2,4-triazoles with BiI_3 yielded three layered inorganic–organic hybrids $[HL1]_4[Bi_6I_{22}]\cdots[L1]_4\cdot 4H_2O$ (**1**), $[HL2]_4[Bi_6I_{22}]\cdot 6H_2O$ (**2**), $[HL2]_2[Bi_2I_8]\cdots[L2]_2$ (**3**) with optical gaps of 1.77, 1.77 and 2.07 eV, respectively. The structures of **1–3** are constructed from inorganic layers of polynuclear anions of bismuth iodine and organic layers of the substituted 1,2,4-triazoles.

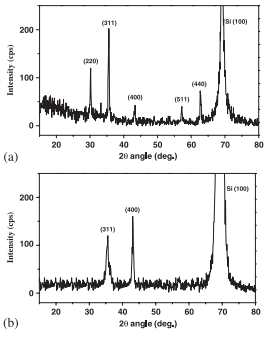

XRD patterns of polycrystalline Fe_3O_4 films growth (a) without and (b) with an external magnetic field.

Regular Articles—Continued

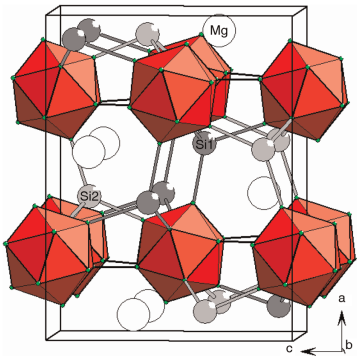

The crystal structure of $MgB_{12}Si_2$, the first ternary compound of the system Mg/B/Si, is characterized by layers of B_{12} icosahedra, connected by isolated Si atoms to a three dimensional framework. Mg atoms are placed in voids of the framework.

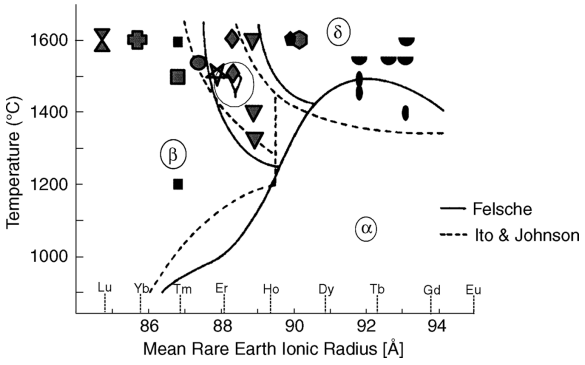

At ambient pressure the phase stabilities not only for pure rare-earth disilicates but also for their solid solutions were found to be strictly related to the simple mean ionic radius.

Continued

Neutron diffraction study and magnetotransport properties of stoichiometric $CaMoO_3$ perovskite prepared by a soft-chemistry route

C. de la Calle, J.A. Alonso, M. García-Hernández and V. Pomjakushin

Page 1636

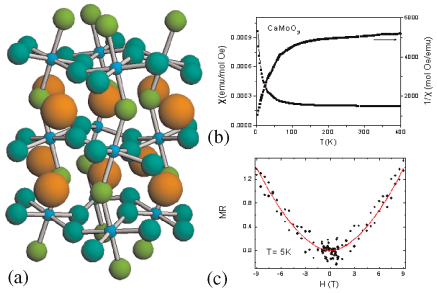

$CaMoO_3$ is an orthorhombic perovskite (*Pbnm*) where the MoO_6 octahedra are tilted by 13.5° (a). It is a Pauli paramagnet (b) and at low temperatures (5 K) presents a small positive magnetoresistance (c).

Crystal growth, transport, and magnetic properties of $Ln_3Co_4Sn_{13}$ (Ln = La, Ce) with a perovskite-like structure

Evan Lyle Thomas, Han-Oh Lee, Andrew N. Bankston, Samuel MaQuilon, Peter Klavins, Monica Moldovan, David P. Young, Zachary Fisk and Julia Y. Chan

Page 1642

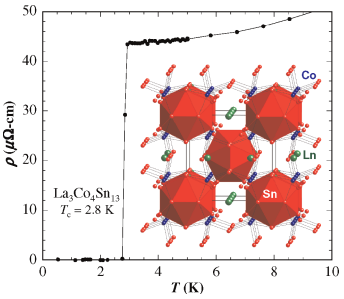

$Ln_3Co_4Sn_{13}$ (Ln = La, Ce) have been grown in single crystalline form from a Sn flux. Their crystal structures are compared to the $A'A''_3B_4O_{12}$-type perovskites. The La compound displays conventional type II superconductivity below $T_c = 2.8$ K. Evidence of a heavy fermionic character is seen in the heat capacity data for the Ce compound which has a large enhanced specific heat coefficient at low temperatures.

High-pressure synthesis, crystal structures, and characterization of $CdVO_{3-\delta}$ and solid solutions $CdVO_3$–$NaVO_3$

Alexei A. Belik and Eiji Takayama-Muromachi

Page 1650

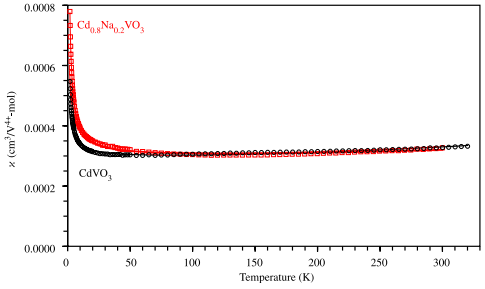

Temperature dependence of the magnetic susceptibilities of $CdVO_3$ and $Cd_{0.8}Na_{0.2}VO_3$.

$Fe_2(AsO_4)F$: A new three-dimensional condensed fluoro-arsenate iron(II) compound with antiferromagnetic interactions

Teresa Berrocal, José L. Mesa, José L. Pizarro, Miren K. Urtiaga, María I. Arriortua and Teófilo Rojo

Page 1659

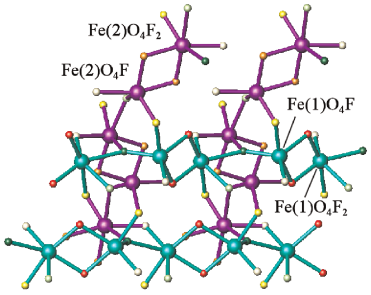

Two types of chain in $Fe_2(AsO_4)F$ showing the five- and hexa-coordination polyhedra.

Synthesis, structure and physical properties of layered semiconductors MCuFCh (M = Sr, Eu, Ch = S, Se)

Eiji Motomitsu, Hiroshi Yanagi, Toshio Kamiya, Masahiro Hirano and Hideo Hosono

Page 1668

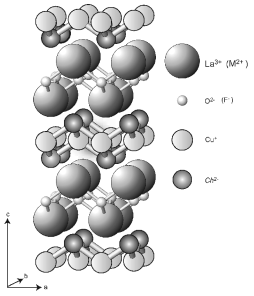

Layered compounds MCuFCh(M = Sr, Eu, Ch = S, Se) were synthesized and their structural, optical, electrical and magnetic properties were measured. The Eu-derivatives exhibit metallic conduction and paramagnetic down to 5 K, while the Sr-derivatives have semiconducting properties with an energy gap of ~3 eV.

Structure and two-dimensional correlation infrared spectroscopy study of two isomeric forms of the octamolybdate cluster

Yiping Chen, Hanhui Zhang, Xuezhen Wang, Changcang Huang, Yanning Cao and Ruiqing Sun

Page 1674

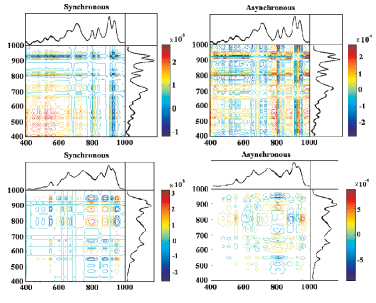

Synchronous and asynchronous correlation spectra of compounds **1** and **2** over a temperature range from 50 to 120 °C in the range of 400–1000 cm^{-1}.

Hydrothermal assembly of (3,6)-connected networks with classical mineral structures constructed from Anderson-type heteropolymolybdate and metal cations
Bo Gao, Shu-Xia Liu, Lin-Hua Xie, Miao Yu, Chun-Dan Zhang, Chun-Yan Sun and Hai-Yan Cheng
Page 1681

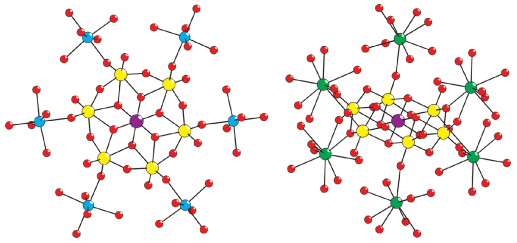

Utilization of mild-hydrothermal synthesis successfully provides a series of new 3D Anderson-based compounds: $(NH_4)_2\{[M(H_2O)_3]_2\ [TeMo_6O_{24}]\}\cdot H_2O$ (M = Mn, Co, Ni, Cu and Zn), which exhibits pyrite-like topology and $[Ln(H_2O)_4]_2\ [TeMo_6O_{24}]\cdot 3H_2O$ (Ln = La, Ce and Nd), which exhibits rutile-like topology.

A low-temperature extraction–solvothermal route to the fabrication of micro-sized MoS_2 spheres modified by Cyanex 301
Huaqiang Shi, Xun Fu, Xiaodong Zhou, Debao Wang and Zhengshui Hu
Page 1690

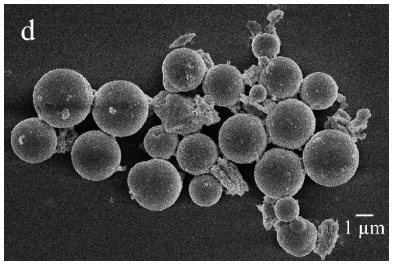

Mono-dispersed MoS_2 micro-spheres with the diameter of 1–3 μm were synthesized in gasoline via extraction–solvothermal method at 150 °C. The MoS_2 product could be well dispersed into organic solvents again and the tribological properties of liquid paraffin (LP) containing MoS_2 micro-spheres were improved.

Microstructural and transport properties in substituted $Bi_2Sr_2CaCu_2O_{8+\delta}$-modulated compounds
C. Autret-Lambert, B. Pignon, M. Gervais, I. Monot-Laffez, A. Ruyter, L. Ammor, F. Gervais, J.M. Bassat and R. Decourt
Page 1698

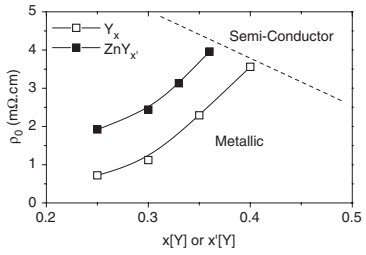

Residual resistivity ρ_0 versus x for both series.

$CuAl_2$ revisited: Composition, crystal structure, chemical bonding, compressibility and Raman spectroscopy
Yuri Grin, Frank R. Wagner, Marc Armbrüster, Miroslav Kohout, Andreas Leithe-Jasper, Ulrich Schwarz, Ulrich Wedig and Hans Georg von Schnering
Page 1707

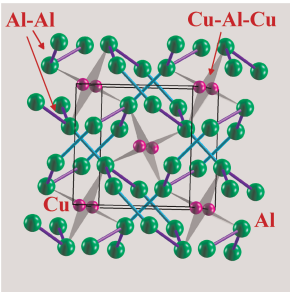

Atomic interactions in the crystal structure of the intermetallic compound $CuAl_2$: Three-bonded aluminum atoms form interpenetrating graphite-like nets. The copper atoms are located in the channels of aluminum network by means of three-center bonds. The bonding model is in agreement with the result of polarized Raman spectroscopy and high-pressure X-ray powder diffraction.

A novel microwave dielectric ceramic $Ca_2Zn_4Ti_{16}O_{38}$: Preparation and dielectric properties
Fei Zhao, Zhenxing Yue, Jing Pei, Zhilun Gui and Longtu Li
Page 1720

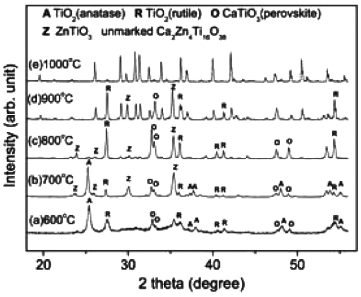

XRD patterns for the $Ca_2Zn_4Ti_{16}O_{38}$ precursor powders after calcining at: (a) 600 °C, (b) 700 °C, (c) 800 °C, (d) 900 °C, and (e) 1000 °C.

Flux syntheses of La-doped $NaTaO_3$ and its photocatalytic activity
Digamber G. Porob and Paul A. Maggard
Page 1727

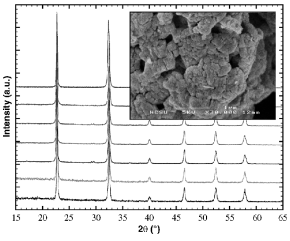

A new molten-salt flux synthesis of La-doped $NaTaO_3$ is reported, which yields aggregates of nanometer-sized particles with irregular block-like morphologies. The flux-synthesized products exhibit an enhanced photocatalytic activity compared to products obtained by conventional solid-state procedures.

Continued

Self-assembly of cerium compound nanopetals via a hydrothermal process: Synthesis, formation mechanism and properties

Yuelan Zhang, Zhitao Kang, Jian Dong, Harry Abernathy and Meilin Liu

Page 1733

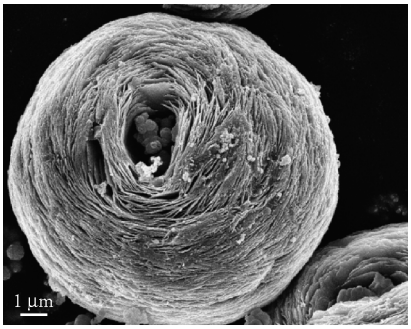

Nanopetals of cerium compounds have been synthesized using a hydrothermal method in a mixed water–ethanol medium. Electron microscopy reveals that each microflower consists of tens to hundreds of cerium hydroxycarbonate nanopetals. These nanopetals have a very large aspect ratio: the thickness is as thin as 10 nm whereas the width is as large as 10 μm. The formation of these unique structures depends strongly on the composition of the precursors, and is attributed to the favored ethanol oxidation by Ce(IV) ions over Ce(IV) hydrolysis.

Synthesis and characterization of two novel pyridine-containing framework gallium ethylenediphosphonates

Zhanhui Yuan, William Clegg and Martin P. Attfield

Page 1739

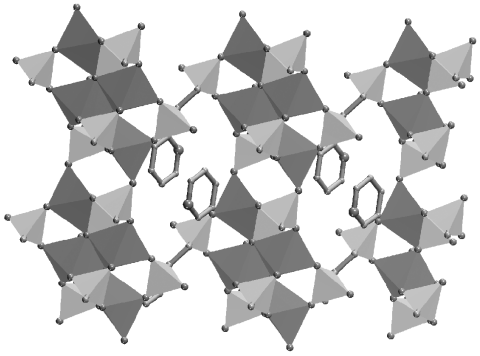

$(C_5H_5N)Ga_3F(O_3PC_2H_4PO_3)_2$ (**I**) and $(C_5H_5NH)_2[Ga_4F_2(O_3PC_2H_4PO_3)_3]$ (**II**) are novel gallium diphosphonate materials composed of Ga-centered polyhedra and ethylenediphosphonate groups that link together to form framework materials with one- and two-dimensional channel systems, respectively. The two structures are formed in the presence of structure-directing pyridine molecules or pyridinium cations and are examples of organically structure-directed framework metal diphosphonates.

Synthesis, structural characterization, and magnetic properties of the antiferromagnetic double perovskites Ln_2LiOsO_6 (Ln = La, Pr, Nd, Sm)

William R. Gemmill, Mark D. Smith and Hans-Conrad zur Loye

Page 1750

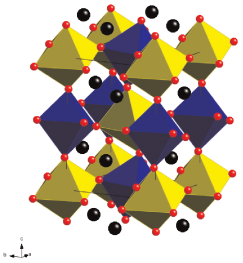

Approximate (110) view of the crystal structure of Pr_2LiOsO_6 (representative of the series Ln_2LiOsO_6 (Ln = La, Pr, Nd, Sm) consisting of OsO_6 octahedra (blue) and LiO_6 octahedra (yello). Praseodymium cations are shown as black spheres and oxygen atoms as red spheres.

A simple method of fabricating large-area α-MnO_2 nanowires and nanorods

Yi Liu, Meng Zhang, Junhao Zhang and Yitai Qian

Page 1757

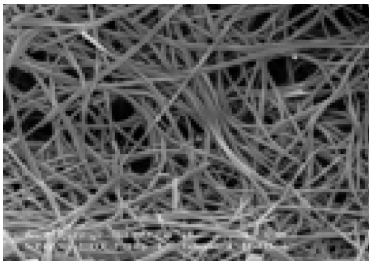

α-MnO_2 nanowires or nanorods have been selectively synthesized via the hydrothermal method in nitric acid condition. The α-MnO_2 nanowires hold with average diameter of 50 nm and lengths ranging between 10 and 40 μm, using $MnSO_4 \cdot H_2O$ as manganese source; meanwhile, α-MnO_2 bifurcate nanorods with average diameter of 100 nm were obtained by adopting $MnCO_3$ as starting material.

Crystal structure and high-pressure properties of γ-Mo_2N determined by neutron powder diffraction and X-ray diffraction

Craig L. Bull, Tetsuya Kawashima, Paul F. McMillan, Denis Machon, Olga Shebanova, Dominik Daisenberger, Emmanuel Soignard, E. Takayama-Muromachi and Laurent C. Chapon

Page 1762

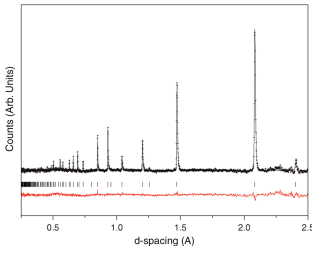

The neutron observed (+), calculated (−) and difference profiles (bottom trace) for γ-MoN at 290 K.

Ferroelectric and dielectric properties of bismuth-layered structural $Sr_2Bi_{4-x}Ln_xTi_5O_{18}$ (Ln = La, Nd, Sm and Dy) ceramics

Feng Qiang, Jun-Hui He, Jun Zhu and Xiao-Bing Chen

Page 1768

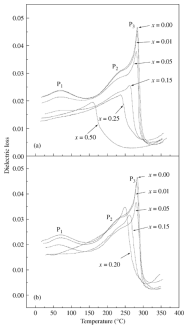

The temperature dependence of the dielectric loss for (a) SBST, and (b) SBDT at 500 kHz.

The Jahn–Teller distortion and cation ordering in the perovskite Sr_2MnSbO_6

Melina Cheah, Paul J. Saines and Brendan J. Kennedy

Page 1775

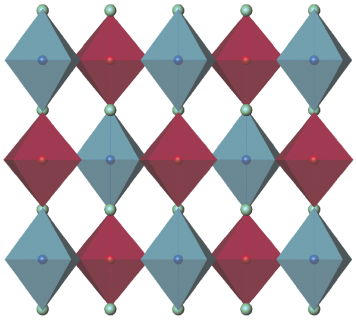

Crystal structure of the tetragonal $I4/m$ structure of Sr_2MnSbO_6 in the 1 0 0 plane. The 0 0 1 view illustrates the effect of tilting of the octahedra and the 1 0 0 view highlights the alternate elongation and compression of the Mn/Sb octahedra. The Mn-rich sites are represented by the blue polyhedra.

A high-temperature structure for Ta_2O_5 with modulations by TiO_2 substitution

Darko Makovec, Jian-Min Zuo, Ray Twesten and David A. Payne

Page 1782

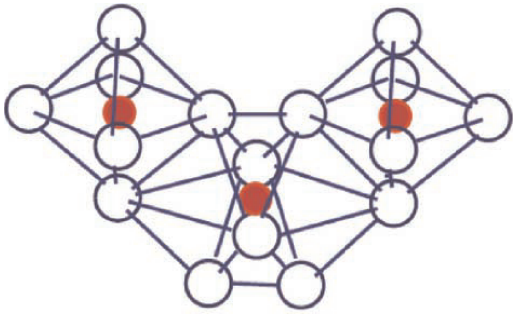

Building block of the proposed structural model for H-Ta_2O_5.

Nanostructural drug-inorganic clay composites: Structure, thermal property and in vitro release of captopril-intercalated Mg–Al-layered double hydroxides

Hui Zhang, Kang Zou, Shaohuan Guo and Xue Duan

Page 1792

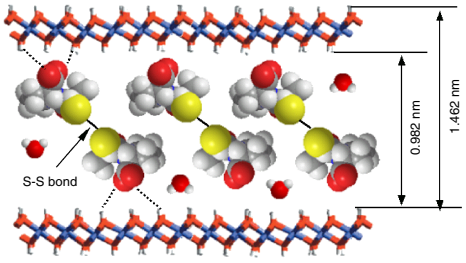

Based on XRD, FT-IR and Raman spectra analyses, it is suggested that captopril (Cpl) exists as its disulphide metabolites in the interlayer of Mg–Al-LDHs via hydrogen bonding between guest carboxylate function and hydroxyl group of the host layers. A schematic supramolecular structure of Cpl intercalates involving a vertical orientation of Cpl disulphide-containing S–S bond between the layers with carboxylate anions pointing to both hydroxide layers is presented.

Titanium-rich highly ordered mesoporous silica synthesized by using a mixed surfactant system

Debraj Chandra, Nawal Kishor Mal, Manabendra Mukherjee and Asim Bhaumik

Page 1802

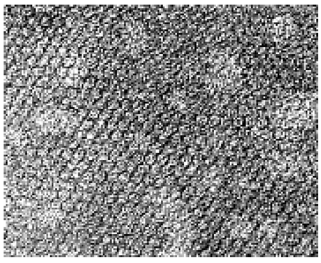

2-D hexagonal mesoporous titanium silicate synthesized by using cationic/non-ionic mixed surfactant system.

Crystal structure, magnetic susceptibility and Mössbauer spectroscopy of the mixed-valence iron phosphate $Na_{1/2}Cu_{4/3}Fe_2(PO_4)_3$

Mourad Hidouri, Besma Lajmi, Alain Wattiaux, Léopold Fournés, Jacques Darriet and Mongi Ben Amara

Page 1808

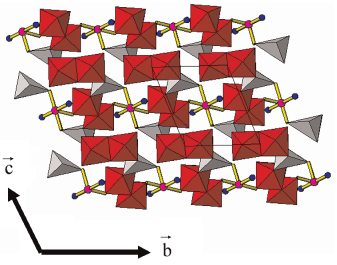

A view of the infinite zigzag chains in the $Na_{1/2}Cu_{4/3}Fe_2(PO_4)_3$ structure.

Continued

Aqueous synthesis of CdTe@FeOOH and CdTe@Ni(OH)$_2$ composited nanoparticles
Liang Li and Jicun Ren
Page 1814

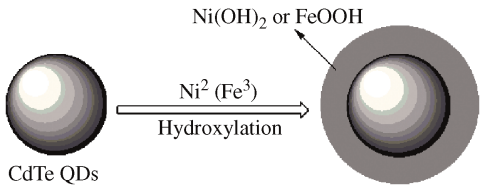

Fluorescent and magnetic bi-functional CdTe@FeOOH and CdTe@Ni(OH)$_2$ nanoparticles were prepared by seed-mediated approach in water phase.

Synthesis of nanocrystals in KNb(Ge,Si)O$_5$ glasses and chemical etching of nanocrystallized glass fibers
Itaru Enomoto, Yasuhiko Benino, Takumi Fujiwara and Takayuki Komatsu
Page 1821

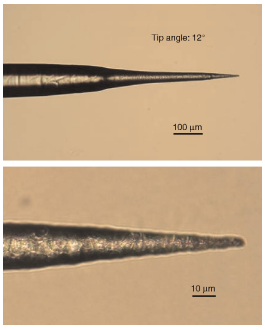

Polarization optical microphotographs for the nanocrystallized glass fiber etched (room temperature, 2 h) chemically using the 10 wt%-HF/hexane system. The glass composition is 25K$_2$O–25Nb$_2$O$_5$–50GeO$_2$.

Incorporation of transition metals into Mg–Al layered double hydroxides: Coprecipitation of cations vs. their pre-complexation with an anionic chelator
Andrey Tsyganok and Abdelhamid Sayari
Page 1830

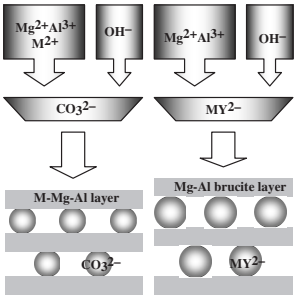

Two ways for introducing transition metals *M*(II) into Mg–Al layered double hydroxides (MY^{2-} denotes the edta chelate of transition metal *M*(II)).

Thermal decomposition of HfCl$_4$ as a function of its hydration state
E. Barraud, S. Bégin-Colin, G. Le Caër, F. Villieras and O. Barres
Page 1842

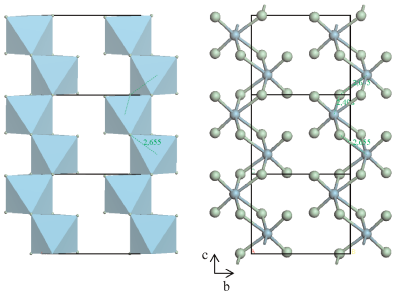

Octahedral chains in ZrCl$_4$ [B. Krebs, Angew. Chem. Int. Ed. 8 (1969) 146–147].

Rapid Communications

Large magnetoresistance in a ferromagnetic cobaltite: The 12H Ba$_{0.9}$CoO$_{2.6}$
A. Maignan, S. Hébert, D. Pelloquin and V. Pralong
Page 1852

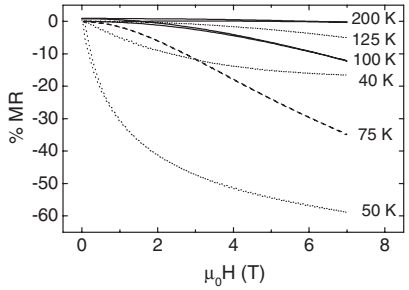

TEM images of (BaTiO(C$_2$O$_4$)$_2$/NH$_2$CONH$_2$) particles show the thickness of shell increasing as the urea addition increases. The enhancement of giant electrorheological activity relates to the increasing interfacial polarization of the core-shell structural (BaTiO(C$_2$O$_4$)$_2$/NH$_2$CONH$_2$).

Oxidation products of the niobium tungsten oxide Nb$_4$W$_{13}$O$_{47}$: A high-resolution scanning transmission electron microscopy study
Frank Krumeich and Reinhard Nesper
Page 1857

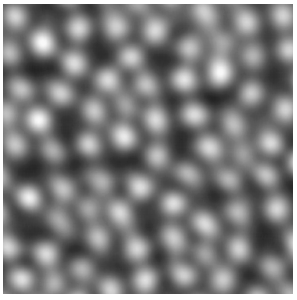

Z contrast image of Nb$_4$W$_{13}$O$_{47}$ oxidized at 1000 °C: Bright dots reveal not only the position of the metal atoms but their intensity provides further information about the distribution of Nb and W.

Oriented growth of $Sr_{n+1}Ti_nO_{3n+1}$ Ruddlesden–Popper phases in chemical solution deposited thin films
Emanuel Gutmann, Alexandr A. Levin, Marianne Reibold, Jan Müller, Peter Paufler and Dirk C. Meyer
Page 1864

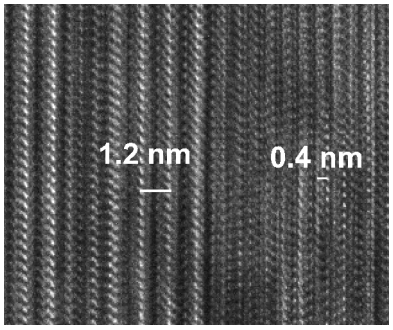

Cross-sectional image of an oriented chemical solution deposited thin film obtained by high-resolution transmission electron microscopy. Periodical spacings corresponding to $SrTiO_3$ substrate (right) and Sr_2TiO_4 Ruddlesden–Popper phase (n=1) film region (left) are marked.

Photoluminescence of new red phosphor $SrZnO_2:Eu^{3+}$
Yuhua Wang and Hui Gao
Page 1870

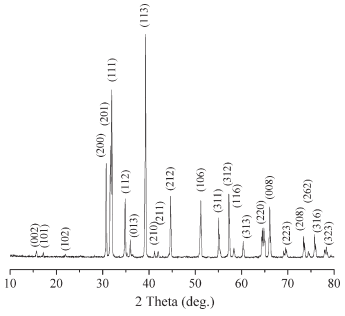

XRD pattern of $SrZnO_2$ sintered at 1000 °C for 2 h.

Electrorheological properties and structure of $(BaTiO(C_2O_4)_2/NH_2CONH_2)$
Jiaxiang Hou, Lei Shi and Qingren Zhu
Page 1874

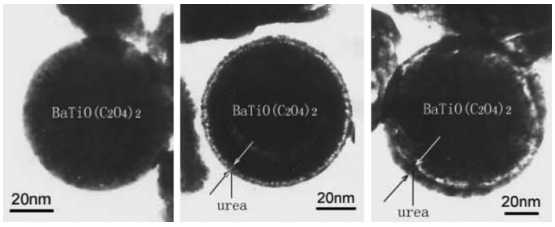

TEM images of $(BaTiO(C_2O_4)_2/NH_2CONH_2)$ particles show the thickness of shell increasing as the urea addition increasing. The enhancement of giant ER activity relate with the increasing interfacial polarization of the core-shell structural $(BaTiO(C_2O_4)_2/NH_2CONH_2)$.

Molten salt synthesis (MSS) of $Cu_2Mo_6S_8$—New way for large-scale production of Chevrel phases
E. Lancry, E. Levi, A. Mitelman, S. Malovany and D. Aurbach
Page 1879

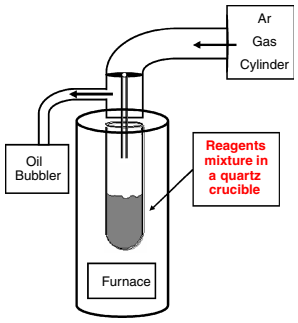

The layout of the molten salt synthesis system.

Synthesis, crystal structure and spectroscopy properties of $Na_3AZr(PO_4)_3$ (A = Mg, Ni) and $Li_{2.6}Na_{0.4}NiZr(PO_4)_3$ phosphates
M. Chakir, A. El Jazouli and D. de Waal
Page 1883

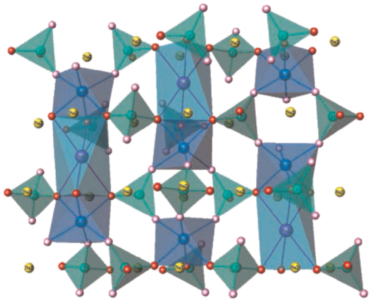

Structure of $Na_3AZr(PO_4)_3$ (A = Mg, Ni) phosphates.

Structural change in a series of protonated layered perovskite compounds, $HLnTiO_4$ (Ln = La, Nd and Y)
Shunsuke Nishimoto, Motohide Matsuda, Stefanus Harjo, Akinori Hoshikawa, Takashi Kamiyama, Toru Ishigaki and Michihiro Miyake
Page 1892

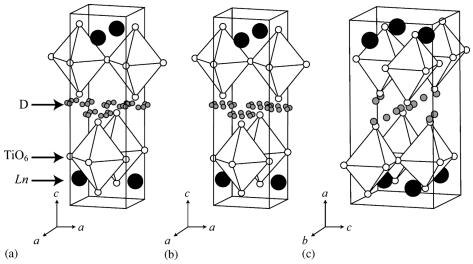

Schematic illustrations of the crystal structures of (a) $DLaTiO_4$, (b) $DNdTiO_4$ and (c) $DYTiO_4$. It is noted that site occupancy factors of D atom in $DLnTiO_4$ (Ln = La and Nd) and $DYTiO_4$ are 1/8 and 1/2 (mean value), respectively.

Continued

Crystal structure of the parent misfit-layered cobalt oxide $[Sr_2O_2]_qCoO_2$
T. Nagai, K. Sakai, M. Karppinen, T. Asaka, K. Kimoto, A. Yamazaki, H. Yamauchi and Y. Matsui
Page 1898

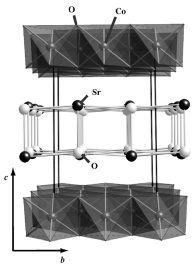

A crystal structure model proposed for the parent misfit-layered cobalt oxide $[Sr_2O_2]_qCoO_2$ ($q = 0.5$) with monoclinic $P2_1/m$ (No. 11) symmetry.

Hydrothermal synthesis, crystal structure and properties of a 3D-framework polyoxometalate assembly: [Ag(4,4′-bipy)](OH){[Ag(4,4′-bipy)]$_2$[PAgW$_{12}$O$_{40}$]} · 3.5H$_2$O
Jian-Xin Chen, Ting-Yan Lan, Yuan-Biao Huang, Chun-Xia Wei, Zhong-Shui Li and Zhi-Chun Zhang
Page 1904

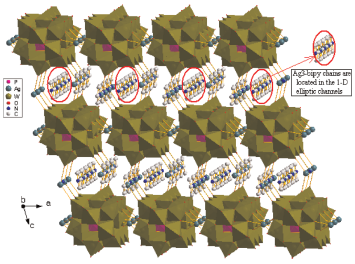

Three-dimensional framework architecture of compound **1** viewed slightly off the *b*-axis showing that 1D Ag3-bipy chains are arranged in the 1D elliptic channels of the framework structure. Water molecules, oxyhydrogen anion and H atoms have been omitted for clarity.

Syntheses, crystal structures and characterizations of BaZn(SeO$_3$)$_2$ and BaZn(TeO$_3$)Cl$_2$
Hai-Long Jiang, Mei-Ling Feng and Jiang-Gao Mao
Page 1911

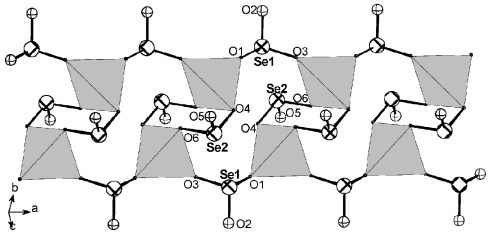

Comparison of 1D double chain of $[Zn(SeO_3)]^{2-}$ along *a*-axis in $BaZn(SeO_3)_2$ with layered $[Zn(SeO_3)_2]^{2-}$ in $SrZn(SeO_3)_2$.

An investigation of the Nd_2O_3–MoO_3 phase system: Thermal decomposition of $Nd_2Mo_4O_{15}$ and formation of $Nd_6Mo_{10}O_{39}$
Rosemary S. Barker and Ivana Radosavljević Evans
Page 1918

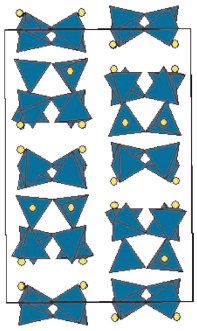

A view of the $Nd_6Mo_{10}O_{39}$ structure.

Preferential occupation of alkaline-earth metal sites in a seemingly disordered solid solution of $Ca_{11-x}Sr_xSb_{10}$: Single crystal structures of $Ca_{8.63(5)}Sr_{2.37}Sb_{10}$ and $Ca_{3.66(7)}Sr_{7.34}Sb_{10}$
Shalabh Gupta and Ashok K. Ganguli
Page 1924

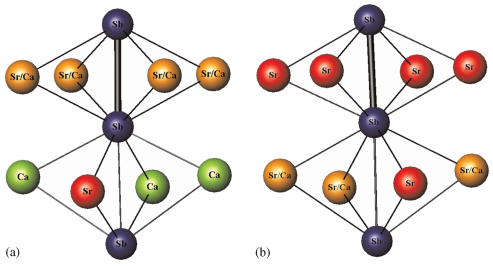

Coordination environment around Sb–Sb dimers in (a) $Ca_{8.63(5)}Sr_{2.37}Sb_{10}$ and (b) $Ca_{3.66(7)}Sr_{7.34}Sb_{10}$. A distinct site preference of alkaline-earth-metal ions depending on the size of the cations has been observed. The anionic sub-structure seems to be playing a crucial role in dictating this site preference.

NOTICE

The Keyword Index for Volume 179 will appear in the December 2006 issue as part of a cumulative index for the year 2006.